

Speckle from branching vasculature: dependence on number density

Kevin J. Parker^{a,*} and Sedigheh S. Pouli^b

^aUniversity of Rochester, Department of Electrical and Computer Engineering,
Rochester, New York, United States

^bUniversity of Rochester, Department of Mechanical Engineering, Rochester,
New York, United States

Abstract

Purpose: Recent theories examine the role of the fractal branching vasculature as a primary site of Born scattering from soft normal tissues. These derivations postulate that the first-order statistics of speckle from soft tissue, such as the liver, thyroid, and prostate, will follow a Burr distribution with a power law parameter that can be related back to the underlying power law, which governs the branching network. However, the issue of scatterer spacing, or the number of cylindrical vessels per sample volume of the interrogating pulse, has not been directly addressed.

Approach: Speckle statistics are examined with a 3D simulation that varies the number density and the governing power law parameter of an ensemble of different sized cylinders. Several *in vivo* liver scans are also analyzed for confirmation across different conditions.

Results: The Burr distribution is found to be an appropriate model for the histogram of amplitudes from speckle regions, where the parameters track the underlying power law and scatterer density conditions. These results are also tested in a more general model of rat liver scans in normal versus abnormal conditions, and the resulting Burr parameters are also found to be appropriate and sensitive to underlying scatterer distributions.

Conclusions: These preliminary results suggest that the classical Burr distribution may be useful in the quantification of scattering of ultrasound from soft vascularized tissues and as a tool in tissue characterization.

© 2020 Society of Photo-Optical Instrumentation Engineers (SPIE) [DOI: [10.1117/1.JMI.7.2.027001](https://doi.org/10.1117/1.JMI.7.2.027001)]

Keywords: ultrasound; backscatter; speckle; fractals; Rayleigh; tissue characterization.

Paper 19279R received Oct. 31, 2019; accepted for publication Mar. 23, 2020; published online Apr. 11, 2020.

1 Introduction

The study of speckle statistics from ultrasound interrogation of soft tissues has a long and distinguished history with a number of treatment theories originally proposed in studies of radar and optical scattering from random materials and media. These treatments lead to classical models of the first-order statistics of speckle, including Rayleigh distributions, homodyne-K, and marked regularity models.^{1–9} The key assumptions about random acoustic scatterers within tissues have been commonly linked to cellular and connective tissues, furthermore linked to concepts, such as average scatterer sizes and concentrations.^{10–22} However, recently, we proposed a different framework for analyzing backscatter from soft vascularized tissues, such as the liver, prostate, brain, and thyroid. The key structures are considered to be the branching cylindrical network of fluid-filled channels that have a few percent difference in acoustic impedance from the reference media, which is the tissue parenchyma composed of close-packed cells. The branching fluid networks are self-similar, fractal networks and we hypothesize that the mathematical

*Address all correspondence to Kevin J. Parker, E-mail: kevin.parker@rochester.edu

parameters of the fractal network substantially determine the first- and second-order statistics of backscatter^{23–25} from these tissues.

To date, the effects of cylindrical vessel density (hypervasculatized versus hypovascularized) and the effect of the size of the interrogated sample volume on the resulting first-order statistics have not been examined. Simulations are conducted in k-Wave²⁶ to quantify the effects of these parameters. It appears that the first-order statistics from a model of cylindrical branching vessels will vary smoothly within three different regimes: the sparse regime where there are few vessels per sample volume of the interrogating pulse, an intermediate range where the power law distribution of the vessels dominates, and then, a high vessel density range where the first-order statistics shift toward the classical Rayleigh (fully developed) speckle. These results are compared with a few ultrasound exams from different tissues and at different frequency bands to confirm the multiscale nature of the formulations.

2 Theory

The first-order statistics for the branching vasculature were recently derived.²⁵ Here, we summarize the main points. First, we assume that a broadband pulse propagating in the x direction is given by separable functions:

$$P\left(y, z, t - \frac{x}{c}\right) = G_y(y, \sigma_y)G_z(z, \sigma_z)P_x\left(t - \frac{x}{c}\right). \quad (1)$$

For example, let $G_y(y, \sigma_y) = \exp[-y^2/2\sigma_y^2]$, i.e., Gaussian in the y (and similarly in the z) direction, and where the pulse shape P_x in the x direction is given by

$$P_x(x) = GH_2\left(\frac{x}{\sigma_x}\right) \exp\left[-\left(\frac{x}{\sigma_x}\right)^2\right] = e^{-x^2/\sigma_x^2} \left(\frac{4x^2}{\sigma_x^2} - 2\right), \quad (2)$$

where GH_2 is a second-order Hermite polynomial for the pulse shape with a spatial scale factor of σ_x ,^{27,28} representing a broadband pulse. Its spatial Fourier transform is then as follows:

$${}^{3D}\Im\{P(x, y, z)\} = (4e^{-k_x^2\pi^2\sigma_x^2}k_x^2\pi^{5/2}\sigma_x^3)(e^{-2k_y^2\pi^2\sigma_y^2}\sqrt{2\pi}\sigma_y)(e^{-2k_z^2\pi^2\sigma_z^2}\sqrt{2\pi}\sigma_z), \quad (3)$$

where we use Bracewell's convention²⁹ for the form of the Fourier transform.

Using a 3D convolution model,^{2,30,31} we consider the “dominant” echoes from the pulse interacting with each generation of elements in a branching, fractal, self-similar set of vessels shown in Fig. 1, whose number density follows a power law behavior $N(a) = N_0/a^b$. From these echoes, the histogram of envelopes is determined by summing up over all the fractal branches.

The isotropic spatial and angular distribution of each generation of fractal branching structures is based on a scalable element. Specifically, consider a long fluid-filled cylinder located along the z -direction of radius a :

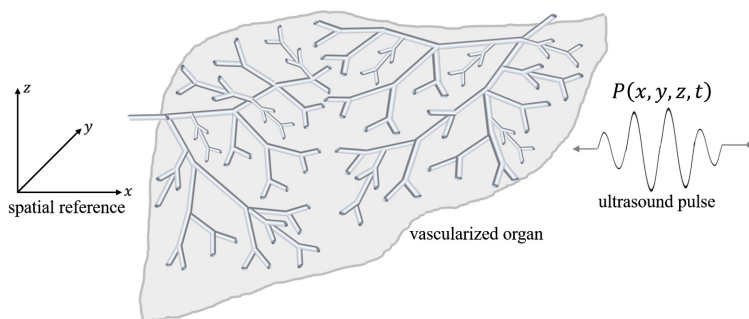


Fig. 1 Model of 3D convolution of a pulse with the fractal branching cylindrical fluid-filled channels in a soft tissue.

$$f(r) = \begin{cases} \kappa_0 & r \leq a \\ 0 & r > a \end{cases}, \quad F(\rho) = \frac{\kappa_0 \cdot a \cdot J_1[2\pi a \cdot \rho]}{\rho}, \quad (4)$$

where κ_0 is the fractional variation in compressibility, where it is assumed that $\kappa_0 \ll 1$, consistent with the Born formulation, $F(\rho)$ represents the Hankel transform, which is the 2D Fourier transform of the radially symmetric function $f(r)$, $J_1[\cdot]$ is a Bessel function of the first kind of order 1, and ρ is the spatial frequency equal to $\sqrt{k_x^2 + k_y^2}$. The fractional variation in compressibility, κ_0 , between blood vessels and liver parenchyma has been estimated to be ~ 0.03 or a 3% difference based on published data.²⁴

The convolution of the pulse with a cylinder of radius a is dominated by the case, where the cylinder is perpendicular to the direction of the forward propagating pulse, the x -axis in our case. Thus, assuming an optimal alignment, the results of the 3D convolution in space, depicted in Fig. 1, are given by the product of the transforms:

$${}^{3D}\mathfrak{F}\{\text{echo}(x, y, z)\} = \mathfrak{F}^{3D}\{p(x, y, z)\} \cdot (k_x)^2 \mathfrak{F}^{3D}\{\text{cylinder}(x, y, z)\}, \quad (5)$$

where the $(k_x)^2$ term premultiplying the cylinder transform stems from the Laplacian spatial derivative in the Born scattering formulation^{32,33} and in the 3D convolution model.^{2,34} In our case, using the 3D spatial Fourier transforms for the pulse [Eq. (3)] and the perpendicular cylinder [Eq. (4)], and inserting them into Eq. (5), we have on the right side of the equation:

$$\left((4e^{-k_x^2 \pi^2 \sigma_x^2} k_x^2 \pi^{5/2} \sigma_x^3) \left(e^{-2k_y^2 \pi^2 \sigma_y^2} \sqrt{2\pi \sigma_y} \right) \left(e^{-2k_z^2 \pi^2 \sigma_z^2} \sqrt{2\pi \sigma_z} \right) \right) \cdot (k_x)^2 \kappa_0 \left(a \left[\frac{1}{\sqrt{k_x^2 + k_y^2}} \right] \cdot \left(J_1 \left[2a\pi \sqrt{k_x^2 + k_y^2} \right] \right) \right) \delta[k_z], \quad (6)$$

where the delta function in k_z stems from the fact that the cylinder is long in the z -direction. We can then assess the total energy in the echo as a function of the parameters by applying Parseval's theorem, where the integral of the square of the transform equals the integral of the square of the echo, and after integration over the delta function in k_z coordinate:

$$\iiint \{\text{echo}(x, y, z)\}^2 dx dy dz = \sigma_z^2 \kappa_0^2 \int_{k_x=-\infty}^{\infty} \int_{k_y=-\infty}^{\infty} (8e^{-\pi^2(k_x^2 \sigma_x^2 + 2k_y^2 \sigma_y^2)} k_x^2 \pi^{7/2} \sigma_x^3 \sigma_y)^2 \cdot (k_x^2)^2 \left(a \left[\frac{1}{\sqrt{k_x^2 + k_y^2}} \right] \cdot \left(J_1 \left[2\pi a \sqrt{k_x^2 + k_y^2} \right] \right) \right)^2 dk_x dk_y. \quad (7)$$

The square root of this gives the root mean square (RMS) amplitude of the echo from a single cylinder as a function of the radius a . We also assume that this RMS amplitude from each echo corresponds to a proportionally higher maximum value of the envelope, as a function of cylinder radius a , denoted as $A[a]$.

From this framework and numerical evaluation of Eq. (7) over a range of realistic parameters, we found²⁵ an approximation, which will be useful for deriving a closed form solution of the echo amplitude for any single long cylinder of radius a , $A[a] = A_0 \sqrt{a - a_{\min}}$ for $a > a_{\min}$ and 0 if $a < a_{\min}$. The overall function is justified by the nearly linear increase in the energy term above some minimum threshold, and the asymptotic modulus of $J_1(ak)$ which is proportional³⁵ to $\sqrt{2/(\pi ak)}$ as ak becomes large. Of course, the exact shape is dependent on the particular pulse shape's spectrum and the beam pattern, and so, this square root function for echo amplitude is only a rough approximation.

The parameter a_{\min} depends on the number of factors, including the dynamic range selected (for example, 45 dB) and the radius below which the weak Rayleigh scattering (long wavelength, small a , small κ_0) behavior of the cylinder interacting with the particular pulse transmit signal cannot be distinguished from the noise floor and quantization floor of the receiver.

Now, applying the general theory of transformed distributions,³⁶ we have within the fractal branching ensemble of cylinders the number density of vessels at different radii given by

$N[a] = N_0/a^b$. We treat this as equivalent to the probability that the incident pulse will encounter a cylinder of radius a , and this can be transformed into the probability distribution of amplitudes $A(a)$. The general rule for transformations is as follows:

$$N[A] = \frac{1}{dA/da} N[a]. \quad (8)$$

In our case, the derivative $dA/da = [(1/2)A_0]/\sqrt{a - a_{\min}}$, and the inverse function is $a[A] = (A/A_0)^2 + a_{\min}$. Thus, substituting these into Eq. (8), the probability distribution of the amplitude $N[A]$ is

$$N[A] = \frac{2N_0 A}{A_0^2[(A/A_0)^2 + a_{\min}]^b}. \quad (9)$$

So, for example, if $b = 2$ and A_0 and N_0 are unity, then $N[A] = 2A/(A^2 + a_{\min})^2$, and this is plotted in Fig. 2 along with variations in parameters.

This provides a four-parameter fit $\{N_0, A_0, a_{\min}, b\}$ to a histogram taken from a reasonably sized region of interest (ROI) within a vascularized tissue or organ. The ROI size must encompass a range of cylindrical vessel radii, from large to small, and within the assumption of an isotropic and spatially uniform distribution of vessels across the ROI.

However, of these four parameters, N_0 , A_0 , and a_{\min} are influenced by system parameters, such as amplifier gain and the size of the ROI. To simplify the analysis, one can normalize the distribution by its integral $\int N[A]dA = N_0/[(b-1)(a_{\min})^{b-1}]$ to form a proper probability density function (PDF), which integrates to unity:

$$N_n[A] = \frac{2A(a_{\min})^{b-1}(b-1)}{A_0^2 \left[\left(\frac{A}{A_0} \right)^2 + a_{\min} \right]^b}. \quad (10)$$

Furthermore, by substituting $\lambda = A_0\sqrt{a_{\min}}$, we find this reduces to a two-parameter distribution:

$$N_n[A] = \frac{2A(b-1)}{\lambda^2 \left[\left(\frac{A}{\lambda} \right)^2 + 1 \right]^b}, \quad (11)$$

which is a Burr type XII distribution^{37,38} with $c = 2$. Thus, the normalized distribution offers a simplification to a two-parameter distribution with analytic expressions for PDF, cumulative distribution function, and moments.³⁸ For example, the peak of the distribution occurs at $A = \lambda/\sqrt{2b-1}$ for $b > 1/2$.

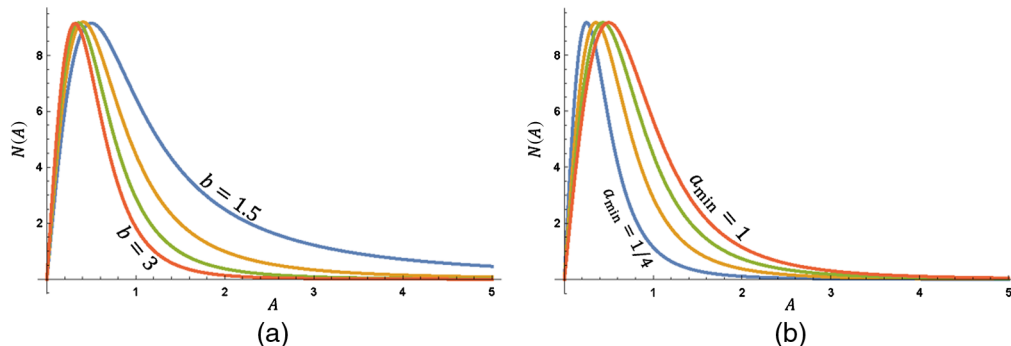


Fig. 2 The proposed histogram function of envelope amplitudes A , having the form $A/(A^2 + a_{\min})^b$. (a) Normalized functions, where $a_{\min} = 1/2$ and the power law parameter b is 3, 2.5, 2, and 1.5, are shown. (b) Normalized functions where the power law parameter is fixed at 2.5, however, a_{\min} is varied as 1/4, 1/2, 3/4, and 1. Vertical axis: counts (arbitrary units); horizontal axis: envelope amplitude (arbitrary units).

Thus, we argue that the Burr distribution [Eq. (11)] is the expected histogram distribution of echo amplitudes from a fractal branching set of Born cylinders. In particular, the power law parameter b is a major parameter of interest.

3 Methods

The numerical simulations are achieved using k-Wave to simulate the time-domain propagation of compressional wave in 3D. k-Wave is an open-source toolbox developed in MATLAB that solves the acoustic wave equations using the k-space pseudospectral method.²⁶

In this study, the simulation domain is a 3D block of 15 mm (in depth, x) \times 13 mm (in the lateral direction, y) \times 3 mm (in the transverse direction, z). It is uniformly divided into small grid elements of $\sim 69.4 \mu\text{m}$ in the x , y , and z directions. The 3D orientation of the transducer for simulation is shown in Fig. 3(a). A few cylindrical branches are also shown here for the clarification of the random branching orientation in the domain.

The medium consists of a uniform background and a set of cylindrical branches with different radii ranging from one to six grid elements mimicking the scattering structures as vessels. The centers of the cylinders are distributed randomly in the x - y plane of Fig. 3(b) using the uniform random distribution function in MATLAB, with an added step to ensure that there is no overlap among any two branches generated. The cylindrical branches are placed along the transverse direction (z) perpendicular to the direction of propagation (x) since the orientation provides the dominant echoes accounted for in our theory.²⁵ The round cylindrical shapes in the model are not exact due to the discretization of radii to grid elements; flat surfaces may appear in some areas on the surface of cylindrical branches. Since flat walls are not realistic and result in strong reflective surfaces, the cylindrical radii are perturbed randomly to avoid the effect of artificially flat boundaries.

Each cylindrical branch is also assigned a specific radius a according to a number density of $N(a)$ in the medium prescribed by the fractal branch power law relation as $N(a) = N_0/a^b$. In this study, three sets of different simulations are performed, each based on the value that is picked for the power law parameter b from the physiological ROI ($2 < b < 3$): $b = 2.2$, 2.5 , and 2.8 . For each set, N_0 is varied from 100 to 400 in increments of 50, guaranteeing that for each N_0 , there is at least one cylinder with the largest radius using the power law formulae. In Fig. 3(b), a 2D representation of cylindrical branch distributions for the case of $b = 2.8$ and $N_0 = 200$ is shown.

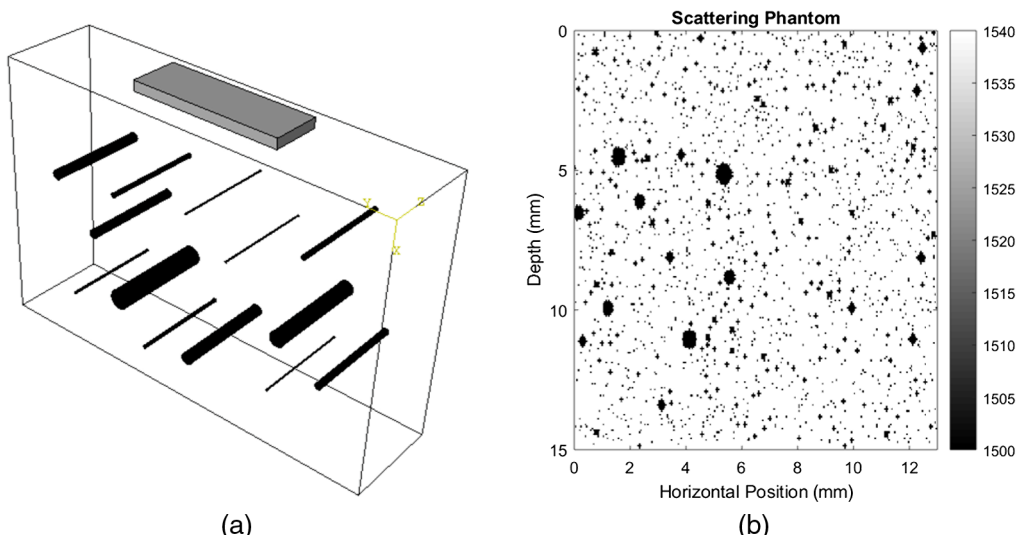


Fig. 3 (a) 3D orientation of the transducer in the simulation domain. A few cylindrical branches are also shown here to illustrate the random branches' orientation in the domain. (b) 2D view (x - y) of the random distribution of cylindrical scatterers shown as black circular spots in the uniform white background, corresponding to the case of $b = 2.8$ and $N_0 = 200$.

Table 1 Physical properties of the transducer in the simulation.

Transducer properties	Value
Number of elements	32
Focus	10 mm
Element width	0.0694 mm
Element height	1.597 mm
Elevation focus	10 mm
Kerf	0

Two cycles with a frequency of 4 MHz are applied as the tone-burst excitation signal using a virtual linear array transducer defined in k-Wave that serves as both source and sensor to the transmit signal and the receive reflection signal, respectively. The transducer is focused at a depth of 10 mm from the top surface of the domain. The center frequency of 4 MHz is applied to mimic the frequency used in tissue scans. Other physical properties of the transducer are listed in Table 1. To avoid side lobe effects, the element width of the transducer satisfies the following condition:

$$\text{element width} \leq \frac{\lambda}{2}, \quad (12)$$

where λ is the wavelength.

The properties of the medium defined here are speed of sound, density, and absorption coefficients. As the medium is heterogeneous, these are defined as matrices in the size of the entire computational domain and a value is assigned to each single element. For elements in the background and cylindrical branch regions, the speed of sound is set to 1540 and 1500 m/s, respectively. The density is assumed to be uniform throughout the entire medium, taking the value of 1000 kg/m³. The absorption coefficient is set to a small value.

Computational time step size is set using a Courant–Friedrichs–Lowy (CFL) number smaller than 0.3 to make the simulation stable (CFL = $c_0 dt / dx$).³⁹ The B-mode image of the domain is reconstructed using sum and delay beamforming, frequency filtering, envelope detection, and log compression from the raw RF data.

Separately, experimental results were obtained from liver experiments. Rat experiments were reviewed and approved by the Institutional Animal Care and Use Committee of Pfizer, Inc., Groton Connecticut, where the ultrasound scan was acquired using a Vevo 2100 (VisualSonics, Toronto, Canada) scanner and a 21-MHz center frequency transducer (data provided courtesy of Terry Swanson). Parameter estimation was performed using MATLAB (MathWorks, Inc., Natick, Massachusetts) nonlinear least-squares minimization of error for two-parameter fits of the Burr distribution to the data.

4 Results

A range of simulations was evaluated with the cylindrical scatterer density parameters varied between a power law b of 2.2, 2.5, and 2.8 and N_0 of 100, 200, 300, and 400. Visually, the results shown in Fig. 4 demonstrate the higher density of scatterers with increasing N_0 . The envelope of the return echoes from these different simulations indicates progressive shifts as the number density of scatterers changes.

In Fig. 5, single A-line envelopes are taken from the center vertical line in the simulations of Fig. 4. At the lowest scatterer density, the envelope has many regions at or near zero. However, as the density increases, the behavior indicates more and higher local maxima with sharp speckle minima that indicate complex summations of nearby scattering sites.

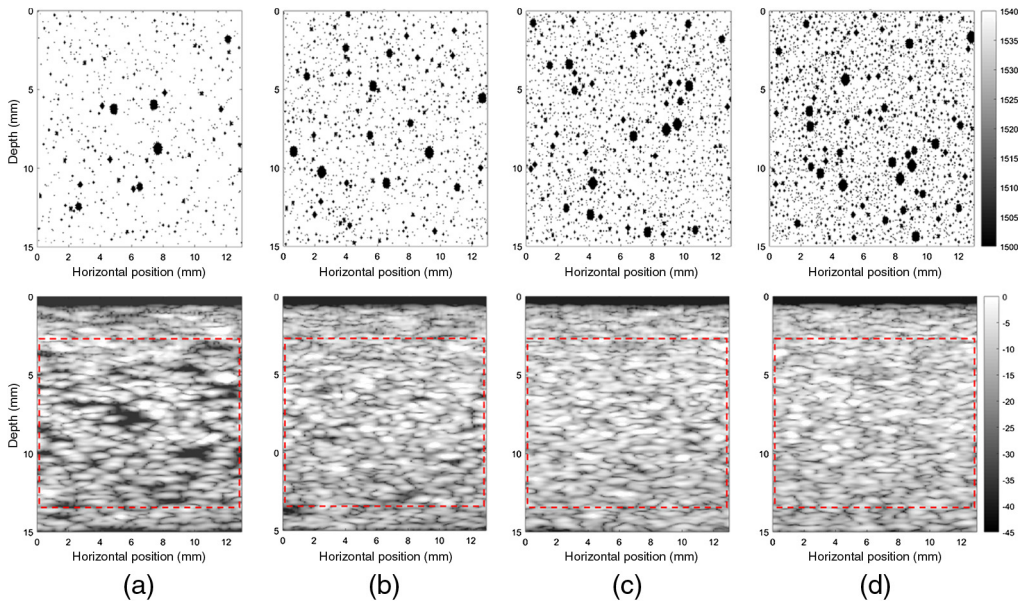


Fig. 4 Comparison of the random scattering fields (top row) and corresponding B-mode images (bottom row) for different number densities based on the power law equation for $b = 2.5$. Column (a) $N_0 = 100$, column (b) $N_0 = 200$, column (c) $N_0 = 300$, and column (d) $N_0 = 400$. A ROI (dashed lines) is shown for analysis.

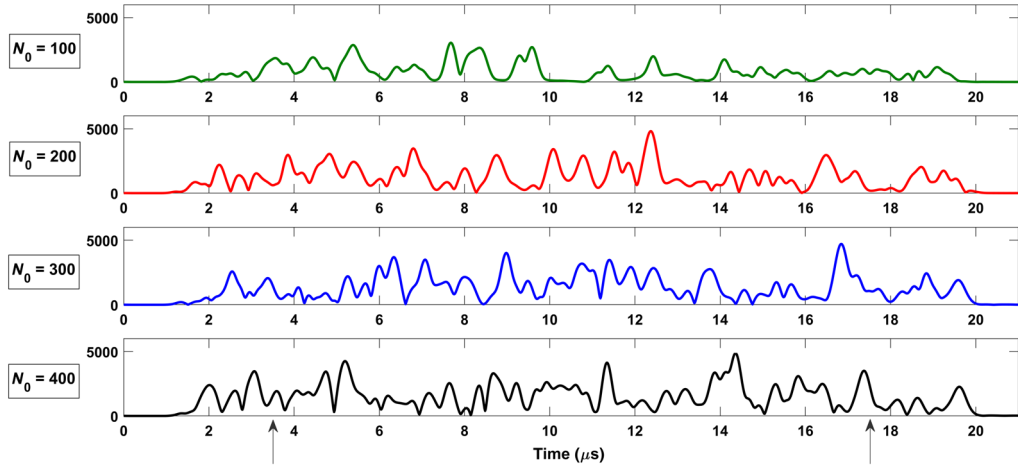


Fig. 5 Envelope plots along the middle line for the power law parameter $b = 2.5$. The two arrows indicate the length of the ROI from which the histogram plots are obtained.

The histograms for three of these cases are shown in Fig. 6 as three samples out of all of the simulations done, showing the Burr-fitted curves and the corresponding fitting parameters. The case of $N_0 = 100$ is not shown because the excess amount of signal at or near zero creates a poor curve fit to Eq. (11); large anechoic regions are not accounted for in the theory.

A summary of all results over the parameter space is given in Fig. 7, also indicating the range of results found over 10 independent simulations of identical parameters. The clear trend is for an increasing fit of the power law estimate \hat{b} not only with the generating power law b but also with the number density of scatterers. This may be explained in Table 2, which reports the average number of scattering cylinders that would lie within the volume of the interrogated pulse. The sample volume produced by the 4-MHz pulse was found to be roughly elliptical with a -10 dB area of $\sim 0.26 \text{ mm}^2$, averaged over the ROI. When the average is less than 1, there are significant

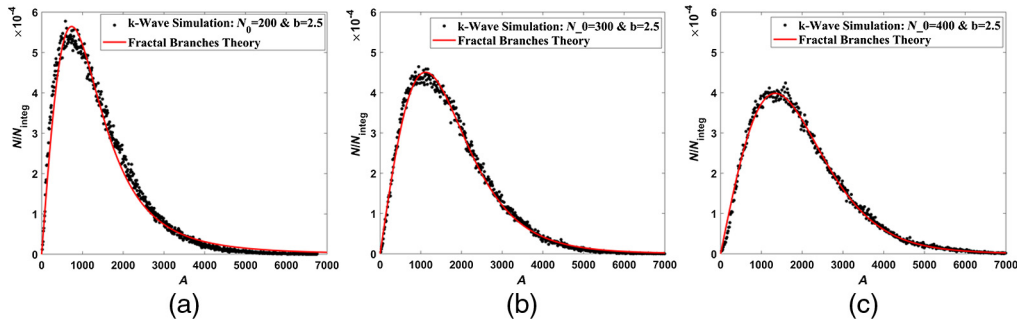


Fig. 6 Fractal branches curve-fitting for: (a) $N_0 = 200$ and $b = 2.5$. Curve-fit parameters: $\hat{b} = 2.341$, $\lambda = 1412$. Goodness of fit: $R^2 = 0.9869$, root mean square error (RMSE) = 0.2088. (b) $N_0 = 300$ and $b = 2.5$. Curve-fit parameters: $\hat{b} = 4.048$, $\lambda = 2980$. Goodness of fit: $R^2 = 0.9954$, RMSE = 0.1059. (c) $N_0 = 400$ and $b = 2.5$. Curve-fit parameters: $\hat{b} = 5.593$, $\lambda = 4280$. Goodness of fit: $R^2 = 0.996$, RMSE = 0.08801.

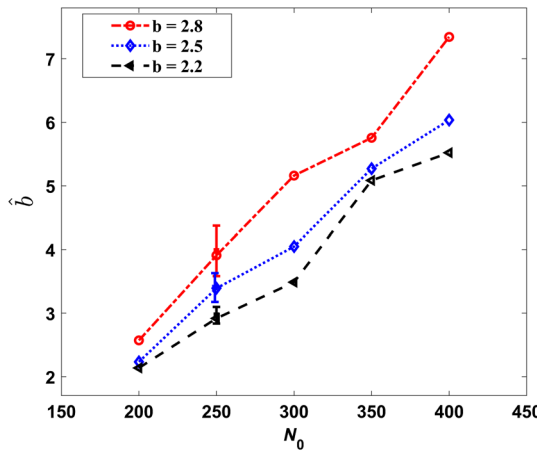


Fig. 7 Summary of simulation results using the fractal branches theory for comparison of results for fitted \hat{b} . Error bars for fitting parameter are also shown when $N_0 = 250$ and $b = 2.2, 2.5$, and 2.8, each resulting from 10 repetitions of the simulation.

Table 2 Averaged number of scatterers within pulse area in k-Wave simulations.

	Variable	$N_0 = 100$	$N_0 = 200$	$N_0 = 300$	$N_0 = 400$
$b = 2.2$	Number of cylinders/pulse	0.81	1.62	2.43	3.25
$b = 2.5$	Number of cylinders/pulse	0.94	1.88	2.82	3.77
$b = 2.8$	Number of cylinders/pulse	1.11	2.21	3.32	4.43

anechoic regions, however, as the scatterer density per sample volume increases toward 4 or higher, significant complex summations can result, and higher estimates of the power law \hat{b} are obtained from the histogram of the envelopes.

To test the generality of the results, we examine *in vivo* scans from rat liver experiments. A normal liver is shown in Fig. 8 with histogram and fits to a Burr distribution ($\hat{b} = 2.8$), then, in Fig. 9, a fibrotic liver with low fat ($\hat{b} = 2.1$), and finally, in Fig. 10, a fibrotic liver with high fat accumulation in vesicles ($\hat{b} = 3.2$). These examples are not simple manipulations of cylindrical number density, and so, represent more general cases than those shown in simulations. However, the fibrotic mesh can be considered to be an increase (compared to normals) of larger scatterers,

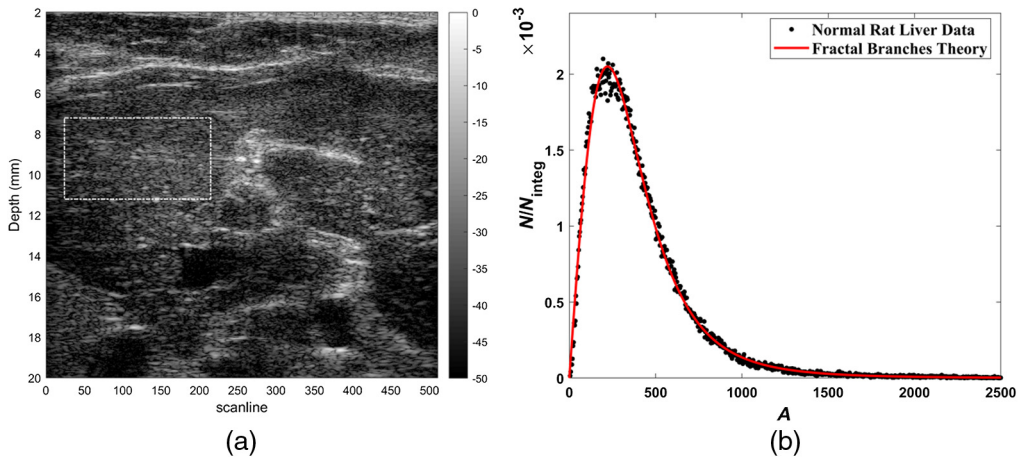


Fig. 8 (a) B-scan image of normal rat liver. A ROI is selected (dashed lines) for analysis. (b) Fractal branching theory fit to the histogram of normalized echo amplitude. Curve-fit parameters: $\hat{b} = 2.832$, $\lambda = 407.1$. Goodness of fit: $R^2 = 0.996$, RMSE = 0.04665.

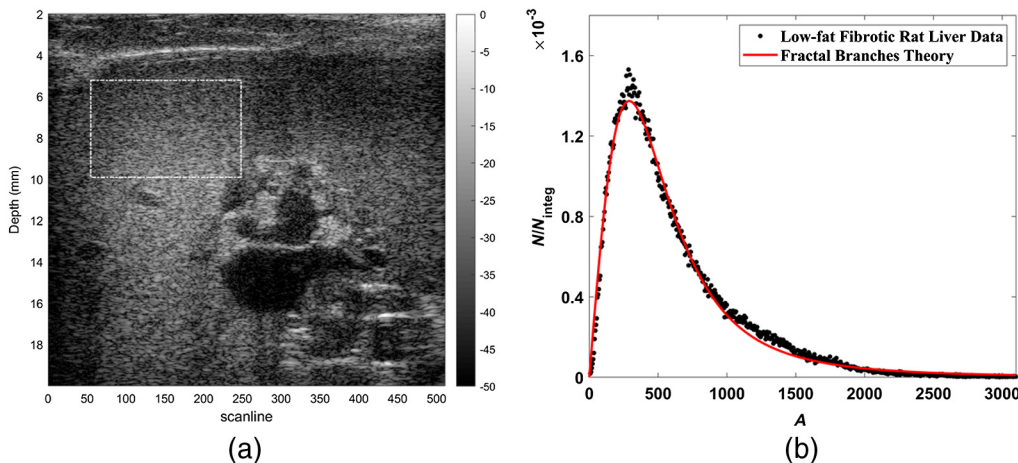


Fig. 9 (a) B-scan image of low fat fibrotic rat liver. A ROI is selected (dashed lines) for analysis. (b) Fractal branching theory fit to the histogram of normalized echo amplitude. Curve-fit parameters: $\hat{b} = 2.184$, $\lambda = 532.5$. Goodness of fit: $R^2 = 0.9933$, RMSE = 0.03381.

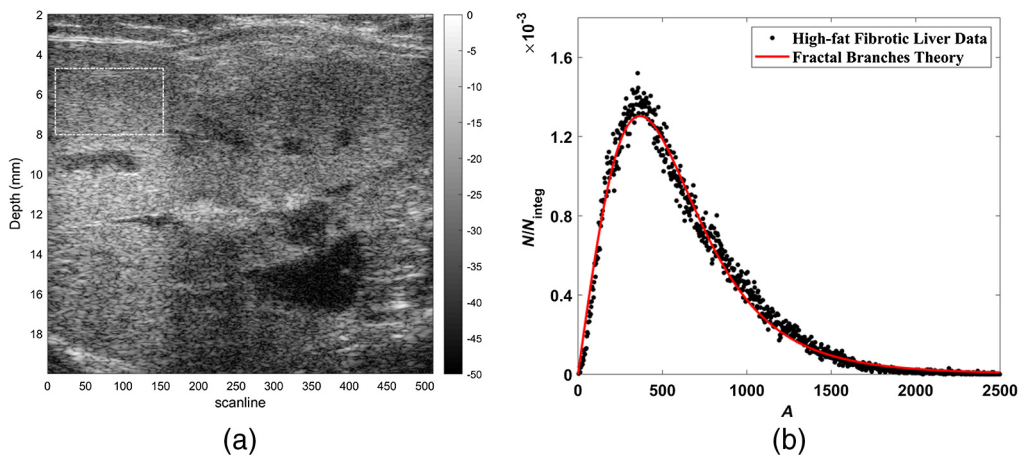


Fig. 10 (a) B-scan image of high fat fibrotic rat liver. A ROI is selected (dashed lines) for analysis. (b) Fractal branching theory fit to the histogram of normalized echo amplitude. Curve-fit parameters: $\hat{b} = 3.219$, $\lambda = 871.8$. Goodness of fit: $R^2 = 0.9878$; adjusted RMSE = 0.04887.

hence, consistent with a lower b (consistent with a number density favoring the larger scatterers). The case with fibrosis and significant accumulation of microvesicular and macrovesicular fat would be consistent with a higher b (favoring a high density of smaller scatterers). Thus, the results indicate some degree of generality of the framework of the Burr distribution, not restricted solely to cylindrical scatterers.

5 Discussion and Conclusion

The derivation leading to the Burr distribution for speckle²⁵ has a number of key assumptions, whereby the accounting of echo amplitudes presumes that each cylindrical vessel at normal incidence to the interrogating pulse contributes according to its own scattering transfer function. There is no accounting for multiple vessels within the sample volume formed by the interrogating pulse, and when these conditions are present, the estimated \hat{b} from the Burr distribution should approximate the underlying power law that governs the fractal branching of the vascular tree. From the numerical simulations, we see this is valid within a zone of scatterer density of between one and two average cylindrical scatterers per sample volume of the interrogating pulse. Below that zone, there are few scatterers and much of the envelopes from a scan line are at or near zero from the asymptotic decay of the echo at long distances from the rare scatterers. This skews the distribution toward lower values of echo amplitudes.

Conversely, when the number density of vessels is so high that there are many within a pulse's volume, then complex summation becomes important. In the classical theory where the random point scatterers are identical and at a number density higher than approximately seven,⁴⁰ then we would expect Rayleigh-distributed envelopes.¹ However, in our framework, the scatterers are not identical, they are sampled from a power law distribution of vessel diameters, and so, the general trend is toward higher values of \hat{b} as more cylinders are included within the pulse sample volume. These overall trends are shown in Fig. 4. As the number density and as b increase within any tissue, the Burr parameters \hat{b} and λ will increase.

We note that the Burr distribution as we derived in Eq. (11) has the denominator term with $(A/\lambda)^2$, and the square term can be traced back in the original derivation to the approximation of how the peak of the echo envelope increases with increasing scatterer size. This result is not precise and can depend on the exact nature of the broadband pulse incident on a cylindrical scatterer. If we allow some perturbation of this, then, the histogram formula can be written as follows:

$$N_{\text{norm}} = \frac{c(b-1)\left(\frac{A}{\lambda}\right)^{c-1}}{\lambda\left[\left(\frac{A}{\lambda}\right)^c + 1\right]^b}, \quad (13)$$

where c is now a third parameter not constrained to 2. This is simply a more general form of the Burr distribution.^{37,38} We have found that this is useful for cases with low N_0 that contain larger anechoic spaces. For example, if the histogram in Fig. 6(a) ($N_0 = 200$) is fit to Eq. (13) instead of Eq. (11), then, we find $c = 1.7$ instead of the assumed 2, and with a higher R^2 (0.99 instead of 0.98). Thus, the three-parameter Burr distribution might have general applicability to a wider range of conditions.

In the liver examples, it is plausible that fibrosis increases the number of larger scatterers (fibrotic patches), whereas fat increases greatly the number of very small (Rayleigh) scatterers. The corresponding changes in \hat{b} as compared with a normal reference case are consistent with these changes in tissue. These results open the possible use of the Burr distribution parameters as biomarkers for tissue vascularity and structural composition.

Disclosures

The authors have no relevant financial interests in the manuscript and no other potential conflicts of interest to disclose.

Acknowledgments

This work was supported by the U.S. National Institutes of Health under Grant No. R21EB025290. The authors also thank Terri Swanson of Pfizer Inc. for providing the RF data from their liver studies.

References

1. C. B. Burckhardt, "Speckle in ultrasound B-mode scans," *IEEE Trans. Sonics Ultrason.* **25**(1), 1–6 (1978).
2. J. C. Bamber and R. J. Dickinson, "Ultrasonic B-scanning: a computer simulation," *Phys. Med. Biol.* **25**(3), 463–479 (1980).
3. G. E. Sleefe and P. P. Lele, "Tissue characterization based on scatterer number density estimation," *IEEE Trans. Ultrason. Ferroelectr. Freq. Control* **35**(6), 749–757 (1988).
4. L. Landini and L. Verrazzani, "Spectral characterization of tissues microstructure by ultrasounds: a stochastic approach," *IEEE Trans. Ultrason. Ferroelectr. Freq. Control* **37**(5), 448–456 (1990).
5. K. A. Wear et al., "Statistical properties of estimates of signal-to-noise ratio and number of scatterers per resolution cell," *J. Acoust. Soc. Am.* **102**(1), 635–641 (1997).
6. R. M. Cramblitt and K. J. Parker, "Generation of non-Rayleigh speckle distributions using marked regularity models," *IEEE Trans. Ultrason. Ferroelectr. Freq. Control* **46**(4), 867–874 (1999).
7. M. A. Kutay, A. P. Petropulu, and C. W. Piccoli, "On modeling biomedical ultrasound RF echoes using a power-law shot-noise model," *IEEE Trans. Ultrason. Ferroelectr. Freq. Control* **48**(4), 953–968 (2001).
8. M. A. Kutay, A. P. Petropulu, and C. W. Piccoli, "Breast tissue characterization based on modeling of ultrasonic echoes using the power-law shot noise model," *Pattern Recognit. Lett.* **24**(4), 741–756 (2003).
9. C. Laporte, J. J. Clark, and T. Arbel, "Generalized Poisson 3-D scatterer distributions," *IEEE Trans. Ultrason. Ferroelectr. Freq. Control* **56**(2), 410–414 (2009).
10. R. C. Chivers, "The scattering of ultrasound by human tissues-some theoretical models," *Ultrasound Med. Biol.* **3**(1), 1–13 (1977).
11. R. C. Waag et al., "Frequency-dependent angle scattering of ultrasound by liver," *J. Acoust. Soc. Am.* **72**(2), 343–352 (1982).
12. F. L. Lizzi et al., "Theoretical framework for spectrum analysis in ultrasonic tissue characterization," *J. Acoust. Soc. Am.* **73**(4), 1366–1373 (1983).
13. J. A. Campbell and R. C. Waag, "Ultrasonic scattering properties of three random media with implications for tissue characterization," *J. Acoust. Soc. Am.* **75**(6), 1879–1886 (1984).
14. R. C. Waag, D. Dalecki, and P. E. Christopher, "Spectral power determinations of compressibility and density variations in model media and calf liver using ultrasound," *J. Acoust. Soc. Am.* **85**(1), 423–431 (1989).
15. R. C. Waag, D. Dalecki, and W. A. Smith, "Estimates of wavefront distortion from measurements of scattering by model random media and calf liver," *J. Acoust. Soc. Am.* **85**(1), 406–415 (1989).
16. M. F. Insana et al., "Describing small-scale structure in random media using pulse-echo ultrasound," *J. Acoust. Soc. Am.* **87**(1), 179–192 (1990).
17. M. F. Insana and D. G. Brown, "Acoustic scattering theory applied to soft biological tissues," in *Ultrasonic Scattering in Biological Tissues*, K. K. Shung and G. A. Thieme, Eds., pp. 75–124, CRC Press, Boca Raton (1993).
18. K. K. Shung and G. A. Thieme, *Ultrasonic Scattering in Biological Tissues*, CRC Press, Boca Raton (1993).
19. D. Savery and G. Cloutier, "A point process approach to assess the frequency dependence of ultrasound backscattering by aggregating red blood cells," *J. Acoust. Soc. Am.* **110**(6), 3252–3262 (2001).
20. I. Fontaine, D. Savery, and G. Cloutier, "Simulation of ultrasound backscattering by red cell aggregates: effect of shear rate and anisotropy," *Biophys. J.* **82**(4), 1696–1710 (2002).

21. D. Savery and G. Cloutier, “Effect of red cell clustering and anisotropy on ultrasound blood backscatter: a Monte Carlo study,” *IEEE Trans. Ultrason. Ferroelectr. Freq. Control* **52**(1), 94–103 (2005).
22. J. Mamou and M. L. Oelze, *Quantitative Ultrasound in Soft Tissues*, Springer, Dordrecht, The Netherlands (2013).
23. K. J. Parker, J. J. Carroll-Nellenback, and R. W. Wood, “The 3D spatial autocorrelation of the branching fractal vasculature,” *Acoustics* **1**(2), 369–381 (2019).
24. K. J. Parker, “Shapes and distributions of soft tissue scatterers,” *Phys. Med. Biol.* **64**(17), 175022 (2019).
25. K. J. Parker, “The first order statistics of backscatter from the fractal branching vasculature,” *J. Acoust. Soc. Am.* **146**(5), 3318–3326 (2019).
26. B. E. Treeby and B. T. Cox, “k-Wave: MATLAB toolbox for the simulation and reconstruction of photoacoustic wave fields,” *J. Biomed. Opt.* **15**(2), 021314 (2010).
27. K. J. Parker, “The H-scan format for classification of ultrasound scattering,” *OMICS J. Radiol.* **5**(5), 1000236 (2016).
28. A. D. Poularikas, Ed., “Transforms and applications handbook,” Chapter 6 in *The Electrical Engineering Handbook Series*, p. 7.21, CRC Press, Boca Raton (2010).
29. R. N. Bracewell, *The Fourier Transform and Its Applications*, Chapter 12, 1st ed., McGraw-Hill, New York (1965).
30. A. Macovski, *Basic Ultrasonic Imaging*, Prentice-Hall, Englewood Cliffs, New Jersey (1983).
31. J. L. Prince and J. M. Links, *Medical Imaging Signals and Systems*, Vol. **2**, [updated] ed., Pearson, Boston (2015).
32. L. Rayleigh, “On the scattering of light spherical shells, and by complete spheres of periodic structure, when the refractivity is small,” *Proc. R. Soc. London Ser. A* **94**(660), 296–300 (1997).
33. P. M. Morse and K. U. Ingard, *Theoretical Acoustics*, Chapter 8, Princeton University Press, Princeton, New Jersey (1987).
34. J. C. Gore and S. Leeman, “Ultrasonic backscattering from human tissue: a realistic model,” *Phys. Med. Biol.* **22**(2), 317–326 (1977).
35. M. Abramowitz and I. A. Stegun, *Handbook of Mathematical Functions with Formulas, Graphs, and Mathematical Tables*, United States Government Printing Office, Washington (1964).
36. A. Papoulis, *The Fourier Integral and Its Applications*, McGraw-Hill, New York (1987).
37. I. W. Burr, “Cumulative frequency functions,” *Ann. Math. Stat.* **13**(2), 215–232 (1942).
38. R. N. Rodriguez, “A guide to the Burr type XII distributions,” *Biometrika* **64**(1), 129–134 (1977).
39. B. E. Treeby et al., “Modelling elastic wave propagation using the k-wave MATLAB toolbox,” in *IEEE Int. Ultrason. Symp.*, pp. 146–149 (2014).
40. T. A. Tuthill, R. H. Sperry, and K. J. Parker, “Deviations from Rayleigh statistics in ultrasonic speckle,” *Ultrason. Imaging* **10**(2), 81–89 (1988).

Kevin J. Parker is the William F. May Professor of Engineering at the University of Rochester. He earned his graduate degrees from Massachusetts Institute of Technology and served at the University of Rochester as department chair, director of the Rochester Center for Biomedical Ultrasound, and dean of engineering/applied sciences. He holds 26 US and 13 international patents (licensed to 25 companies), is the founder of VirtualScopics, and has published more than 220 journal articles. He is a fellow of the IEEE, AIUM, ASA, AIMBE, and NAI.

Sedigheh S. Poul is a PhD degree student in the Department of Mechanical Engineering at the University of Rochester. She received her MS degree from the University of Rochester in August 2019, and her BS degree from the University of Tehran, Iran, in 2014, both in mechanical engineering. Her research interests include ultrasound elastography, tissue characterization, viscoelasticity, and finite-element modeling.